Outer membrane *c*-type cytochromes OmcA and MtrC play distinct roles in enhancing the attachment of *Shewanella oneidensis* MR-1 cells to goethite

Xinxin Jing[1,#], Yichao Wu[1,#], Liang Shi[2,3], Caroline L. Peacock[4], Noha Mohamed Ashry[1,5], Chunhui Gao[1], Qiaoyun Huang[1], Peng Cai*[,1]

1 State Key Laboratory of Agricultural Microbiology, College of Resources and Environment, Huazhong Agricultural University, Wuhan, China

2 Department of Biological Sciences and Technology, School of Environmental Studies, China University of Geosciences, Wuhan, China

3 State Key Laboratory of Biogeology and Environmental Geology, China University of Geosciences, Wuhan, China

4 School of Earth and Environment, University of Leeds, Leeds LS2 9JT, UK

5 Agriculture Microbiology Department, Faculty of Agriculture, Benha University, Moshtohor, Qalubia, 13736, Egypt

# The authors contributed equally to this work. Author order was determined by level of contribution.

Running head: Roles of OmcA and MtrC in cell-goethite interaction

*Corresponding author: Peng Cai, cp@mail.hzau.edu.cn

ABSTRACT

The outer membrane *c*-type cytochromes (*c*-Cyts) OmcA and MtrC in *Shewanella* are key terminal reductases that bind and transfer electrons directly to iron (hydr)oxides. Although the amount of OmcA and MtrC at the cell surface and their molecular structures are largely comparable, MtrC is known to play a more important role in dissimilatory iron reduction. To explore the roles of these outer membrane *c*-Cyts in the interaction of *S. oneidensis* MR-1 with iron oxides, the attachment processes of *S. oneidensis* MR-1 wild type and *c*-type cytochrome-deficient mutants (Δ*omcA,* Δ*mtrC* and Δ*omcA*-Δ*mtrC*) to goethite are compared via quartz crystal microbalance with dissipation monitoring (QCM-D). Strains with OmcA exhibit a rapid initial attachment. The quantitative model for QCM-D responses reveals that MtrC enhances the contact area and contact elasticity of cells with goethite by more than one and two times, respectively. *In situ* ATR-FTIR 2D-CoS analysis shows that MtrC promotes the initial interfacial reaction via an inner-sphere coordination. AFM analysis demonstrates that OmcA enhances the attractive force between cells and goethite by about 60%. As a result, OmcA contributes to higher attractive force with goethite and induces a rapid short-term attachment, while MtrC is more important in the longer-term interaction, through an enhanced contact area, which promotes interfacial reactions. These results reveal *c*-Cyts OmcA and MtrC adopt different mechanisms for enhancing the attachment of *S. oneidensis* MR-1 cells to goethite. It improves our understanding of the function of outer membrane *c*-Cyts and the influence of cell surface macromolecules in cell-mineral interactions.

IMPORTANCE

Shewanella species are one group of versatile and widespread dissimilatory iron-reducing bacteria, which are capable of respiring insoluble iron minerals via six multiheme c-type cytochromes. Outer membrane *c*-type cytochromes (*c*-Cyts) OmcA and MtrC are the terminal reductases in this pathway which share comparable protein structures. In this study, we elucidate the different roles of OmcA and MtrC in the interaction of *S. oneidensis* MR-1 with goethite at the whole-cell level. OmcA confers enhanced affinity towards goethite and results a rapid attachment. Meanwhile, MtrC increases the contact area of bacterial cells with goethite significantly and promotes the interfacial reaction which may explain its central role in extracellular electron transfer. This study provides novel insights into the role of bacterial surface macromolecules in the interfacial interaction of bacteria with minerals, which is critical to develop a comprehensive understanding of cell-mineral interactions.

Keywords: *Shewanella oneidensis*; outer-membrane *c*-type cytochromes; attachment; iron oxide; QCM-D

INTRODUCTION

Microbial dissimilatory iron reduction (DIR) plays an important role in soil and sediment biogeochemistry (1). Under oxic conditions, iron is largely present as ferric iron, that at typical soil and sediment pH is precipitated as iron (hydr)oxide minerals (2). Under anoxic conditions, these (hydr)oxides can serve as terminal electron acceptors and are thus reduced to ferrous iron species, coupled to the oxidation of organic carbon (1). This redox process mediates the biogeochemical cycling of iron and carbon, but also impacts the reactivity and cycling of other essential bioelements and contaminants, through control of subsurface redox conditions (3).

Although microbial cell envelopes are impermeable to iron minerals, microbes have evolved various mechanisms to facilitate extracellular electron transfer (4, 5). *Shewanella* species are one group of versatile and widespread metal (hydr)oxide-reducing bacteria, which are capable of respiring insoluble iron minerals via six multiheme *c*-type cytochromes (6). These cytochromes located in membranes and periplasmic space transfer electrons across the cell envelope to mineral surfaces. Outer membrane *c*-type cytochromes (*c*-Cyts) OmcA and MtrC are the terminal reductases in this pathway, which contact and exchange electrons with extracellular minerals directly. When lacking these outer membrane *c*-Cyts, *S. oneidensis* MR-1 is unable to proliferate on iron mineral surfaces under anoxic conditions (7, 8).

Due to the indispensable role of outer membrane *c*-Cyts in extracellular electron transfer, both their distribution and structure at cell surfaces, and their interaction with iron (hydr)oxides have been studied. In particular, previous works show that there is a similar amount of MtrC and OmcA present on *S. oneidensis* MR-1 cell surfaces (9, 10), but antibody

84 recognition suggests that MtrC is uniformly distributed across the cell surfaces, while OmcA
85 is mainly localized at the cell-mineral interface (11). Furthermore, OmcA and MtrC are
86 reported to contain similar structural and heme arrangements (4, 12). In order to transfer
87 electrons to minerals directly, OmcA and MtrC contain a conserved binding motif
88 (Ser/Thr-Pro-Ser/Thr) via which hydrogen bonds form between serine residues and
89 hydroxylated iron (hydr)oxide surfaces (13). The crystal structure of OmcA places the binding
90 motif near heme 10, which brings the electron egress site to about 10 Å of mineral surface
91 (14). Accordingly, force measurements with atomic force microscopy (AFM) reveal the
92 strength of the bond between OmcA and hematite is approximately twice as strong as the
93 MtrC-hematite bond (15).

94 Although the amount of OmcA and MtrC at the cell surface and their protein structures
95 are reportedly largely comparable, their functions during cell-mineral interactions appear to
96 be different. In this regard, most studies to date have used purified *c*-Cyts to elucidate the role
97 of outer membrane *c*-Cyts in bacteria-mineral interactions (14-19), but a limited number of
98 studies with whole cells of *S. oneidensis* MR-1 reveal that the mutant strain lacking MtrC is
99 less able to reduce iron (hydr)oxide than strains lacking OmcA, which suggests that MtrC
100 plays a more dominant role than OmcA in extracellular electron transfer and iron (hydr)oxide
101 reductive dissolution (8, 20, 21). Although their different contributions to extracellular
102 electron transfer may be attributed to the close association of MtrC to the transmembrane
103 complex MtrAB, the potentially different roles of OmcA and MtrC in the attachment of
104 *Shewanella* cells onto iron oxides at the whole cell level remain largely unknown.

105 The objective of this study was to explore the roles of *c*-Cyts (OmcA and MtrC) in the

interaction of *S. oneidensis* MR-1 with the common soil and sediment iron (hydr)oxide goethite. A quartz crystal microbalance with dissipation monitoring (QCM-D) was used to compare the dynamic attachment processes of *S. oneidensis* MR-1 wild type (WT) and outer membrane *c*-type cytochrome deleted mutants (lacking OmcA, Δ*omcA,* lacking MtrC, Δ*mtrC,* and lacking both OmcA and MtrC, Δ*omcA*-Δ*mtrC*). The QCM-D responses were fitted to a quantitative model to describe the underlying mechanical properties of attachment. Molecular-level processes were characterized by using attenuated total reflectance Fourier transform infrared (ATR-FTIR) spectroscopy. Atomic force microscopy (AFM) analysis was further employed to examine the direct interaction force between *S. oneidensis* MR-1 and goethite. This study provides novel insights into the role of bacterial surface macromolecules in the interfacial interaction of bacteria with minerals, which is critical to develop a comprehensive understanding of cell-mineral interactions and how these help control subsurface redox and biogeochemical conditions.

RESULTS

QCM-D Attachment Behaviour of *S. oneidensis* MR-1 to Goethite. QCM-D was applied to investigate the role of outer membrane *c*-Cyts in the dynamics of *S. oneidensis* MR-1 attachment on goethite. Upon the introduction of bacterial cells to the goethite surface, the dissipation shift (ΔD) initially increases rapidly during the first 3 hours of attachment, after this decreases rapidly during the next 1 hour of attachment, and then gradually approaches a constant value after 4 hours of attachment (Fig. 1). Based on the changes of ΔD, the entire attachment processes can be divided into three stages.

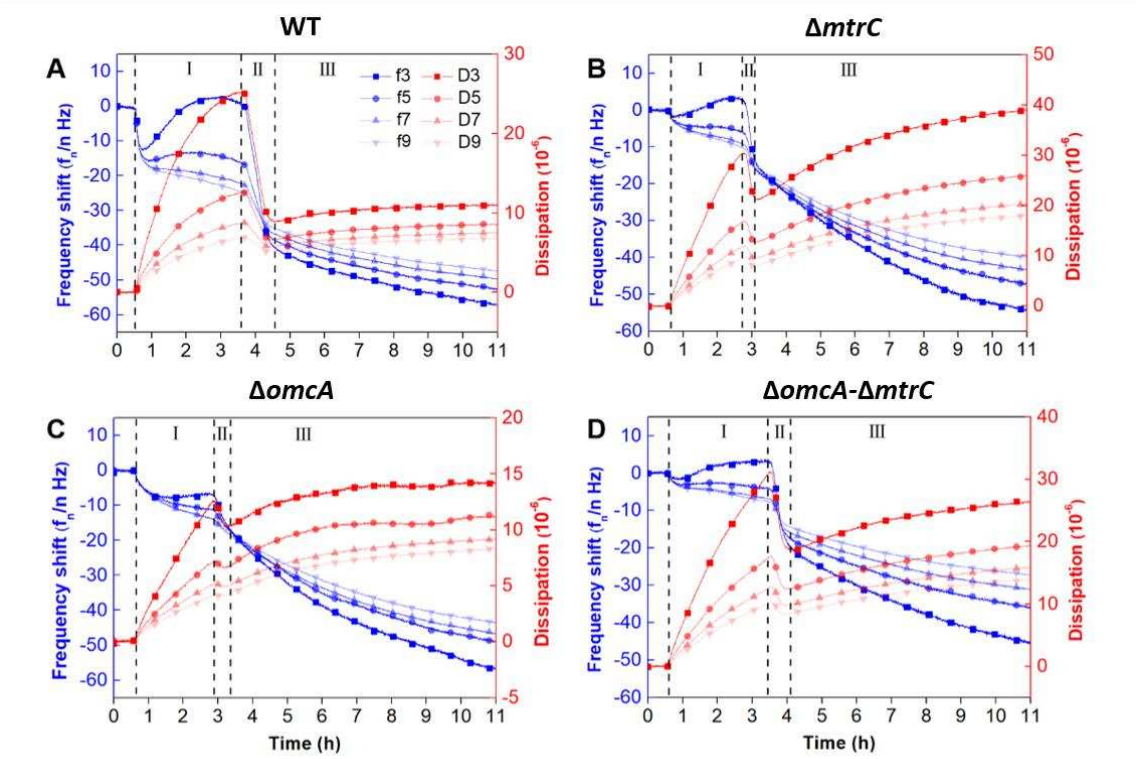

Fig. 1. The frequency (Δf) and dissipation (ΔD) shift for the attachment of WT (A), Δ*mtrC* (B), Δ*omcA* (C) and Δ*omcA*-Δ*mtrC* (D) on goethite-coated QCM-D sensors. I, II and III are different stages of bacterial attachment based on the changes of ΔD. f_n and D_n indicate the frequency and dissipation at 4 different overtones.

In the first stage, ΔD of both the WT and mutants increases but the frequency shifts (Δf) vary between different strains, especially at the 3rd overtone (Δf_3) (Fig. 1). Specifically, the Δf_3 of WT (Fig. 1A) and the mutant lacking MtrC, Δ*mtrC* (Fig. 1B) decrease and then increase gradually, reaching a peak with increasing ΔD. This trend in Δf_3 indicates there is considerable bacterial attachment. Meanwhile, there are negligible changes in Δf for the mutant lacking OmcA, Δ*omcA*, and lacking both OmcA and MtrC, Δ*omcA*-Δ*mtrC*, indicating there is less bacterial attachment (Fig. 1C and D). These results agree with the microscope images, in that WT and Δ*mtrC* have a comparable amount of attached cells at the end of the first stage (7.1± 0.7 vs. 6.4±0.3×10^6 cells/cm^2) (Fig. 2), but Δ*omcA* and Δ*omcA*-Δ*mtrC* have significantly less attached cells, the surface cell densities of which are less than 50% of that of WT ($P < 0.01$). It should be noted that although an increased mass loading on the QCM sensor resulting from bacterial attachment to the goethite surface usually leads to a negative shift of Δf, a positive shift of Δf at the 3rd overtone is observed in the first stage for WT and Δ*mtrC* (Fig. 1). The positive shift of Δf is attributed to the oscillation of the soft bacterial layer, which counteracts the negative frequency shift (22, 23). As the sensing depth of QCM-D decays with $1/\sqrt{n}$ (24), the positive shift of Δf_3 and significant increased ΔD_3 indicate thick soft bacterial layers of WT and Δ*mtrC* develop on the goethite surface.

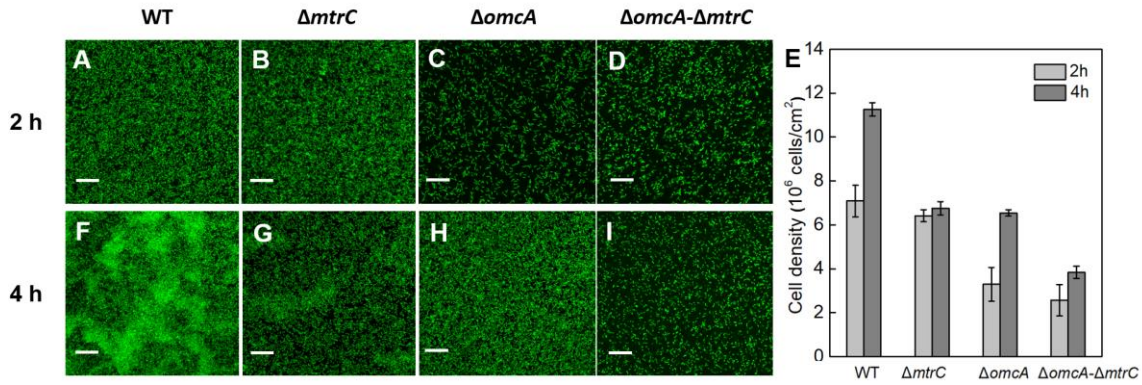

Fig. 2. WT (A, F), Δ*mtrC* (B, G), Δ*omcA* (C, H) and Δ*omcA*-Δ*mtrC* (D, I) after 2 and 4 hour attachment on goethite surfaces. The surface cell density is determined by statistical image analysis (E).

In the second stage, when Δ*D* reaches a peak after 3 hours of attachment, Δ*D* and Δ*f* of the WT and mutants start to decrease simultaneously (Fig. 1). This trend suggests there is a transition in the type and number of bacterial attachments, which may suppress the oscillation of the surface-associated cells and reduce the steric hindrance, thus facilitating further cell attachment. Based on confocal laser scanning microscopy (CLSM) imaging, all the strains except Δ*mtrC* show a substantial increase in the amount of attached cells (Fig. 2). At the end of the second stage, Δ*omcA* and Δ*mtrC* share similar surface cell densities (6.5±0.1 vs. 6.8±0.3×10^6 cells/cm^2), which are significantly higher than those of Δ*omcA*-Δ*mtrC* (3.8±0.3×10^6 cells/cm^2, $P < 0.01$).

In the third stage, Δ*D* and Δ*f* gradually approach to certain values (Fig. 1). Except Δ*omcA*-Δ*mtrC*, no significant increase in bacterial density on the goethite surface is observed (Fig. S1). This indicates that stable bacterial attachment is established after about 4 hours. The Δ*D* and Δ*f* for WT across different overtones are converged to 1×10^{-5} and -50 Hz, respectively,

while the ΔD and Δf for mutants are diverged (Fig. 1). As the penetration depth of the acoustic wave decays with the increase of overtones, the converged ΔD and Δf suggest that WT cells form a homogenous layer on goethite (25). Regarding the mutant strains, the ΔD_3 of Δ*omcA* at 11 hours is much lower than those of Δ*mtrC* and Δ*omcA*-Δ*mtrC*, which suggests a stable attachment with less oscillation.

Modelled Viscoelastic Characteristics of *S. oneidensis* MR-1 Attachment to Goethite. To further investigate the adhesive behaviour of the surface-associated bacteria, the recorded Δf and ΔD at 10 hours is fitted to the quantitative QCM-D model (26). The Δf for WT and the mutant lacking OmcA, Δ*omcA*, show a negative linear correlation with the overtone number (Fig. 3A and C), which suggests the QCM-D signals are dominated by inertial response and can be well-described by the free-oscillating model (upper branch in Fig. 4). As the inertial and elastic loads are connected in parallel (Fig. 4), the reciprocal of the total QCM-D response equals the sum of the reciprocals of inertial and elastic loads. Therefore, these inertial QCM-D responses suggest there is a higher contribution from contact elasticity during bacterial attachment. On the contrary, the Δf of the mutant lacking MtrC, Δ*mtrC*, and lacking both OmcA and MtrC, Δ*omcA*-Δ*mtrC*, deviate from the free-oscillating model, which suggests a non-negligible contribution of inertial interaction (Fig. 3B and D). Based on model fitting, the contact elasticity parameter for WT is the highest, and is 48.7% higher than that of Δ*omcA* (Table 1). The mutant strains lacking MtrC, Δ*mtrC* and Δ*omcA*-Δ*mtrC*, demonstrate 71.4% and 82.0% reduction in contact elasticity compared with WT. These results indicate that the presence of MtrC contributes to elastic interactions between *S. oneidensis* MR-1 and

goethite.

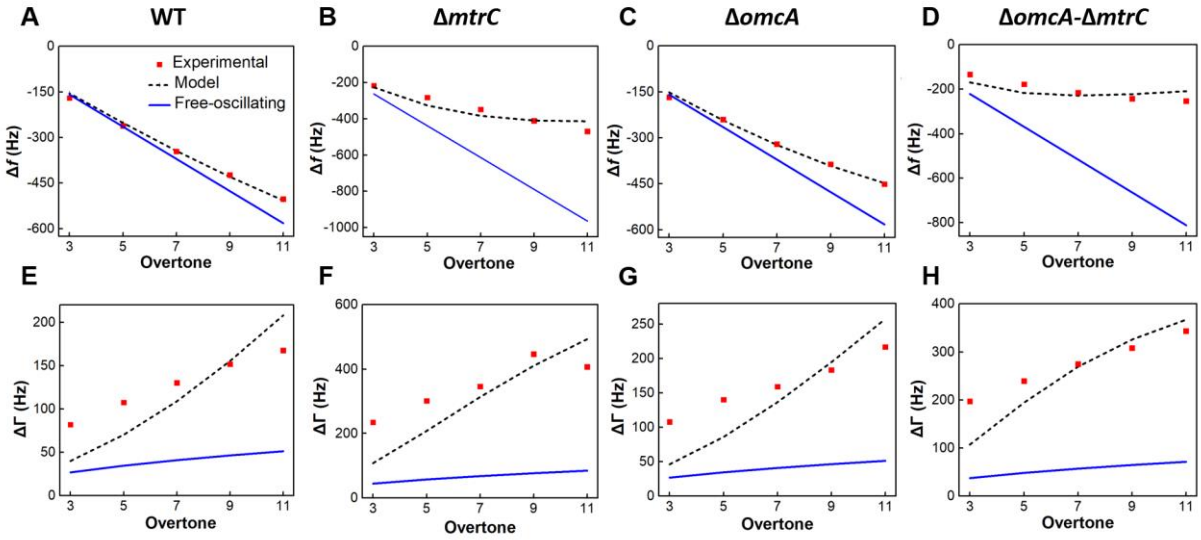

Fig. 3. Experimental and predicted Δf and $\Delta\Gamma$ as a function of the overtone number for WT (A, E), Δ*mtrC* (B, F), Δ*omcA* (C, G) and Δ*omcA*-Δ*mtrC* (D, H).

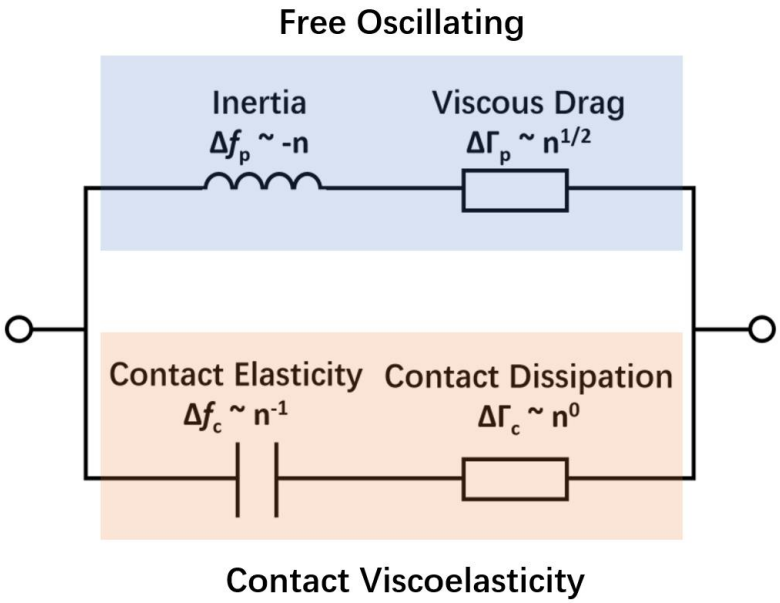

Fig. 4. The proposed equivalent circuits for the load impedance of the crystal associated with

200 a single attached bacterial cell showing the overtone dependence of inertial, viscous, elastic
201 and dissipative loads.
202
203 The bandwidth shift ($\Delta\Gamma$) for all the strains exceeds the free-oscillating model prediction
204 (Fig. 3E-H). This discrepancy suggests the viscosity of the attached bacterial layer
205 significantly contributes to energy dissipation. The positive relationship between $\Delta\Gamma$ and
206 overtone number also highlights the involvement of viscous dissipation, which is expected to
207 correlate with $n^{1/2}$ (Fig. 4). The magnitude of the contact damping parameter follows the same
208 sequence as the elastic coefficient κ_c (WT > Δ*omcA* > Δ*mtrC* > Δ*omcA*-Δ*mtrC*) (Table 1).
209 This is consistent with recent work showing that a higher elastic coefficient is associated with
210 higher damping parameters (26). The contact radius of individual attached cells can be further
211 estimated based on the predicted parameters. WT exhibits the highest contact radius, which
212 reaches 536.37 nm (Table 1), and is more than 1.7-fold higher than that of Δ*omcA*-Δ*mtrC*.
213 Among the mutants, the contact radius of Δ*omcA* is significantly higher than that of Δ*mtrC*.
214 These results suggest that the presence of MtrC enhances the contact area between *S.*
215 *oneidensis* MR-1 and goethite, and that a higher contact area results in higher elastic and
216 damping effects during the cell-mineral interaction. The predicted result is in consistent with
217 the immunolocalization assay. The distribution of MtrC and OmcA on the surface of WT is
218 uniform (Fig. 5A and B). When lacking MtrC, the distribution of OmcA on cell surface
219 becomes heterogeneous. MOC is calculated to evaluate the distribution of outer membrane
220 *c*-Cyts. The overlap coefficient of OmcA in Δ*mtrC* is 22% less than that of WT, while Δ*omcA*
221 shares a comparable MOC with WT. It should be noted that the predicted surface cell

densities (N_p) are one order of magnitude less than those determined from the microscope data (Table 1). The discrepancy could be caused by the small fraction of observed cells that formed a stable contact with the goethite surface (26).

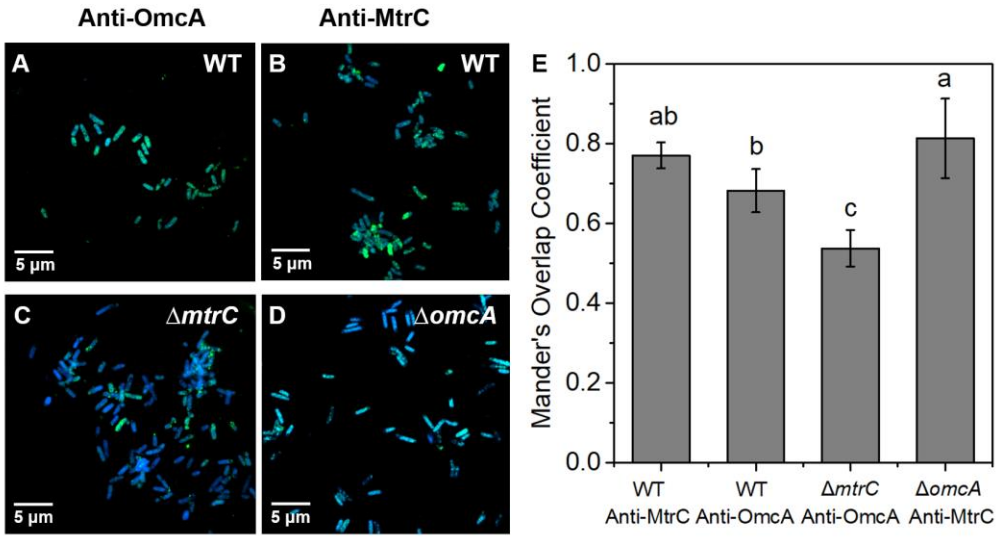

Fig. 5. Immunolocalization images of outer membrane *c*-Cyts OmcA and MtrC on cell surface of WT (A, C), Δ*mtrC* (C), Δ*omcA* (D) stained by DAPI (blue). Outer membrane *c*-Cyts OmcA and MtrC were specific labeled with antibodies against OmcA (A and C, green) or MtrC (B and D, green).

2D-CoS Analysis of the Interaction Sequence of the Bacterial Cell Surface Functional Groups on Goethite. The FTIR spectra of goethite-free *S. oneidensis* strains reveal prominent amide and phosphate bands, including 1081 ($\nu_s(PO_2^-)$), 1235 ($\nu_{as}(PO_2^-)$), 1543 (amide II), and 1654 cm^{-1} (amide I) (Fig. S2 and Table S1). The spectral signatures of WT and mutants are similar, which suggests that the absence of *c*-Cyts does not significantly affect the abundance of the different surface functional groups.

Online *in situ* ATR-FTIR analysis was performed to investigate the role of OmcA and MtrC in bacterial adhesion to goethite at the molecular level. After introduction of bacteria, the intensities of the amide I and II bands increase rapidly (Fig. S3). As amide II is insensitive to structural changes, the area of the amide II band is used as an indicator of the amount of bacterial adhesion (27). Consistent with the QCM-D data, the amide II peak area of WT increases rapidly during the first 2 hours of attachment (Fig. S4), and based on this corroborated behaviour, the surface reaction between the bacteria and goethite is separated into two phases, an initial 2-hour fast attachment and a subsequent longer-term adhesion.

The interaction of bacterial cell surface functional groups with goethite was further resolved via 2D-CoS analysis. In the first 2 hours, the sequence of interaction for WT is as follows (Fig. S5): $\upsilon_s(PO_2^-)$ (1087 cm^{-1}), υ(C−OH/ C−O−C/C−C) (1053 cm^{-1}), υ(P-OFe) (1046 cm^{-1}) > amide I (1645 cm^{-1}), amide II (1543 cm^{-1}) (Table S2). The analysis also resolves the degree of changes in intensity which is as follows: $\upsilon_s(PO_2^-)$ (1087 cm^{-1}) > υ(C−OH/C−O−C/C−C) (1053 cm^{-1}) > amide II (1543 cm^{-1}) > amide I (1645 cm^{-1}). These results indicate that P-moieties which mainly originated from phospholipids, lipopolysaccharide and eDNA are involved in the initial attachment. The phosphate groups exhibited high affinity towards iron oxides through the formation of covalent bonds (28-31). $\upsilon_s(PO_2^-)$ at 1087 cm^{-1} and υ(P-OFe) at 1046 cm^{-1} manifest the formation of inner-sphere monodentate Fe-phosphate/phosphonate surface complexes during initial attachment (32). In the longer-term attachment, the sequential order becomes: υ(C−OH/C−O−C/C−C) (1076 cm^{-1}) > amide II (1546 cm^{-1}) > amide I (1645 cm^{-1}) (Table S3). The intensity follows the sequence: υ(C−OH/C−O−C/C−C) (1076 cm^{-1}) > amide II (1546 cm^{-1}) > amide I (1645 cm^{-1}) >

260 $\upsilon_s(COO^-)$ (1398 cm^{-1}). These results indicate that C-moieties of polysaccharides and surface

261 proteins dominate interfacial interactions during the longer-term attachment.

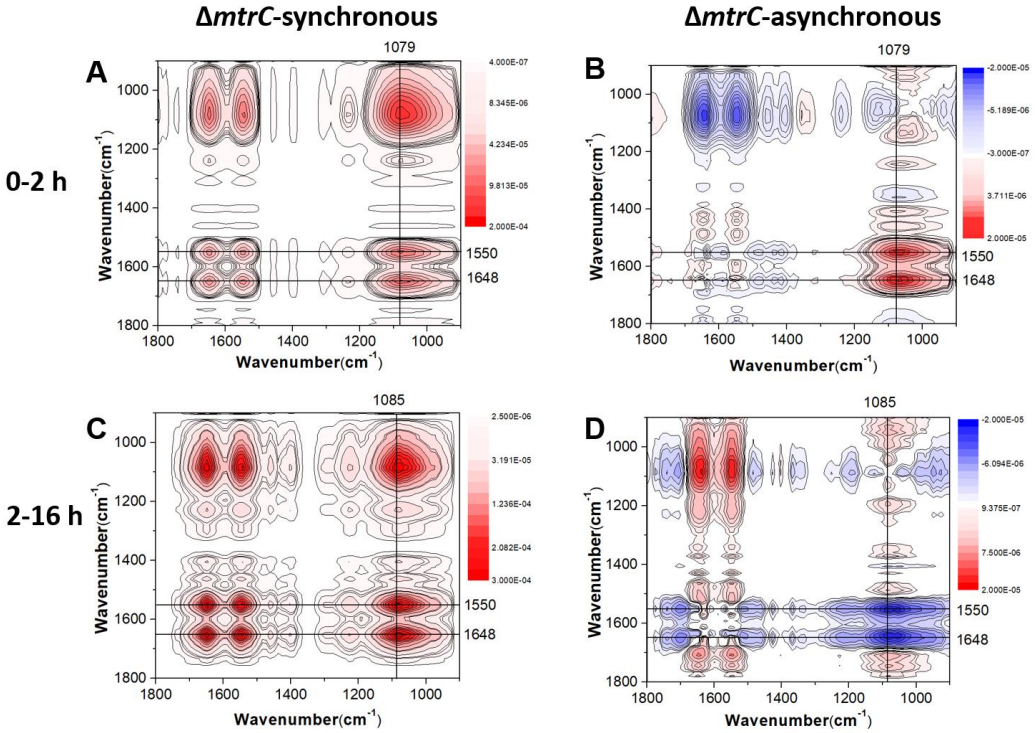

262

263 **Fig. 6.** Synchronous (A, C) and asynchronous (B, D) 2D correlation map of time-dependent

264 ATR-FTIR spectra for the short-term (A, B) and long-term (C, D) attachment of Δ*mtrC* cells

265 to goethite. The red and blue regions represent positive and negative correlation intensities.

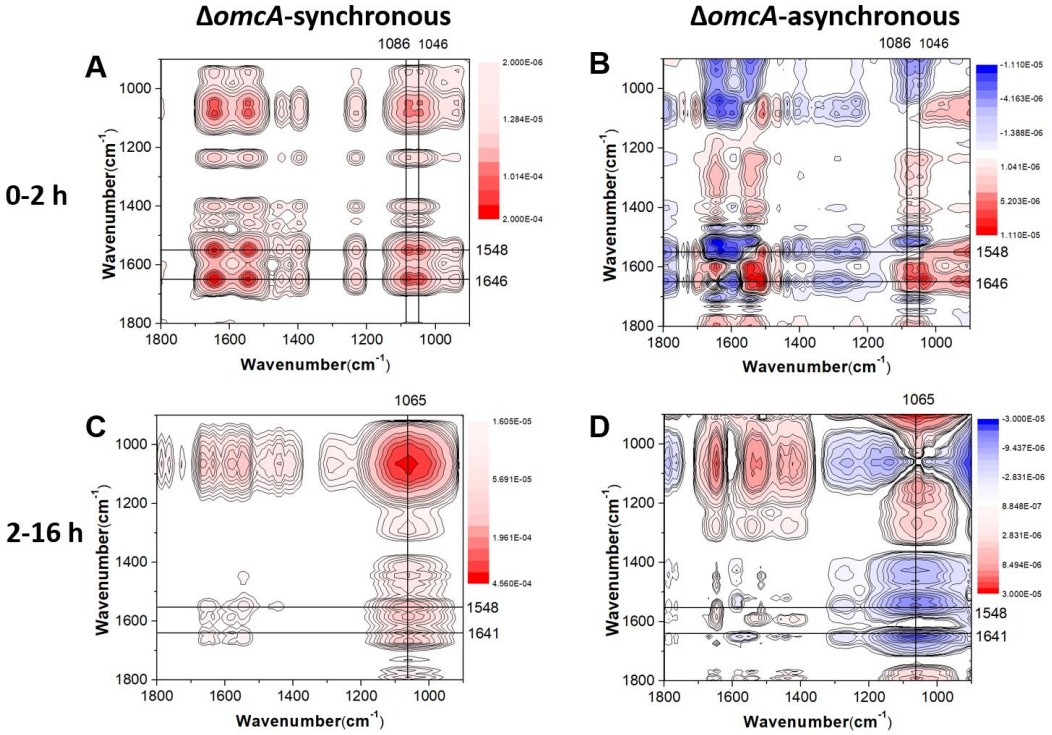

Fig. 7. Synchronous (A, C) and asynchronous (B, D) 2D correlation map of time-dependent ATR-FTIR spectra for the short-term (A, B) and long-term (C, D) attachment of Δ*omcA* cells to goethite. The red and blue regions represent positive and negative correlation intensities.

The deletion of outer membrane *c*-Cyts is found to trigger pronounced differences in the mechanisms of the surface interfacial reactions (Fig. 6, 7 and S6). In the first 2 hours, the sequences of interaction for the mutants lacking MtrC, Δ*mtrC*, and lacking both OmcA and MtrC, Δ*omcA*-Δ*mtrC,* are: $\upsilon_s(PO_2^-)$ (1079 cm^{-1}) > $\upsilon_{as}(PO_2^-)$ (1238 cm^{-1}) > amide II (1550 cm^{-1}) > amide I (1648 cm^{-1}) (Table S4) and υ(C−OH/ C−O−C/C−C) (1051 cm^{-1}), $\upsilon_s(PO_2^-)$ (1082 cm^{-1}) >$\upsilon_s(COO^-)$ (1404 cm^{-1})> amide I (1644 cm^{-1}) >amide II (1548 cm^{-1}), $\upsilon_{as}(PO_2^-)$ (1236 cm^{-1}) (Table S5), respectively. Meanwhile, the sequence of interaction for the mutant lacking OmcA, Δ*omcA*, is: $\delta(CH_3/CH_2)$ (1462 cm^{-1}) > υ(P-OFe) (1046 cm^{-1}), $\upsilon_s(PO_2^-)$ (1086 cm^{-1}), amide II (1548 cm^{-1}) > amide I (1646 cm^{-1}) > $\upsilon_s(COO^-)$ (1400 cm^{-1}) (Table S6). These

results demonstrate that during the initial attachment stage, WT and Δ*mtrC* attach to the goethite surface via P-moieties $\upsilon_s(PO_2^-)$ (Fig. S5 and 6), while WT and Δ*omcA* form inner-sphere monodentate Fe-phosphate/phosphonate surface complexes, υ(P-OFe) (1046 cm^{-1}) (Fig. S5 and 7), which are absent for Δ*mtrC* (Fig. 6) and Δ*omcA*-Δ*mtrC* (Fig. S6). The longer-term attachment process for Δ*omcA* (Table S7) is also analogous to that of WT, in which C-moieties of polysaccharides and surface proteins dominate the surface reactions. In the longer-term attachment process for Δ*mtrC* (Table S8) and Δ*omcA*-Δ*mtrC* (Table S9), both polysaccharides and proteins are involved, but also the phosphate groups contribute to the binding via formation of monodentate bonds ($\upsilon_s(PO_2^-)$ (1085 cm^{-1}), $\upsilon_{as}(PO_2^-)$ (1226 cm^{-1})). Overall, these results suggest that MtrC contributes to the initial interfacial reaction between *S. oneidensis* MR-1 and goethite via an inner-sphere coordination between cell surface phosphate groups and the goethite surface.

AFM Analysis of the Mechanical Features of *S. oneidensis* MR-1 Adhesion to Goethite. Colloidal probe AFM was used to investigate the interaction force between *S. oneidensis* strains and goethite. The largest adhesion force is observed for WT and the mutant lacking MtrC, Δ*mtrC*, upon retraction. The attractive force was 1.17 ± 0.05 nN (mean ± standard error, n=100) for WT and 1.18 ± 0.05 nN for Δ*mtrC* (Fig. 8A and B). Meanwhile when lacking OmcA, the adhesion force for Δ*omcA* and Δ*omcA*-Δ*mtrC* are significantly reduced to 0.71±0.03 and 0.75±0.03 nN, respectively (Fig. 8C and D). The weak attraction force of Δ*omcA* and Δ*omcA*-Δ*mtrC* also corresponds to shorter rupture lengths (Table S10). The distance over which the attractive interaction between WT and goethite occurs is more

than twice that for Δ*omcA*-Δ*mtrC* ($P < 0.05$). The rupture length of Δ*mtrC* is shorter than that of WT, but still significantly longer compared to mutants deficient in OmcA ($P < 0.05$) (Table S10).

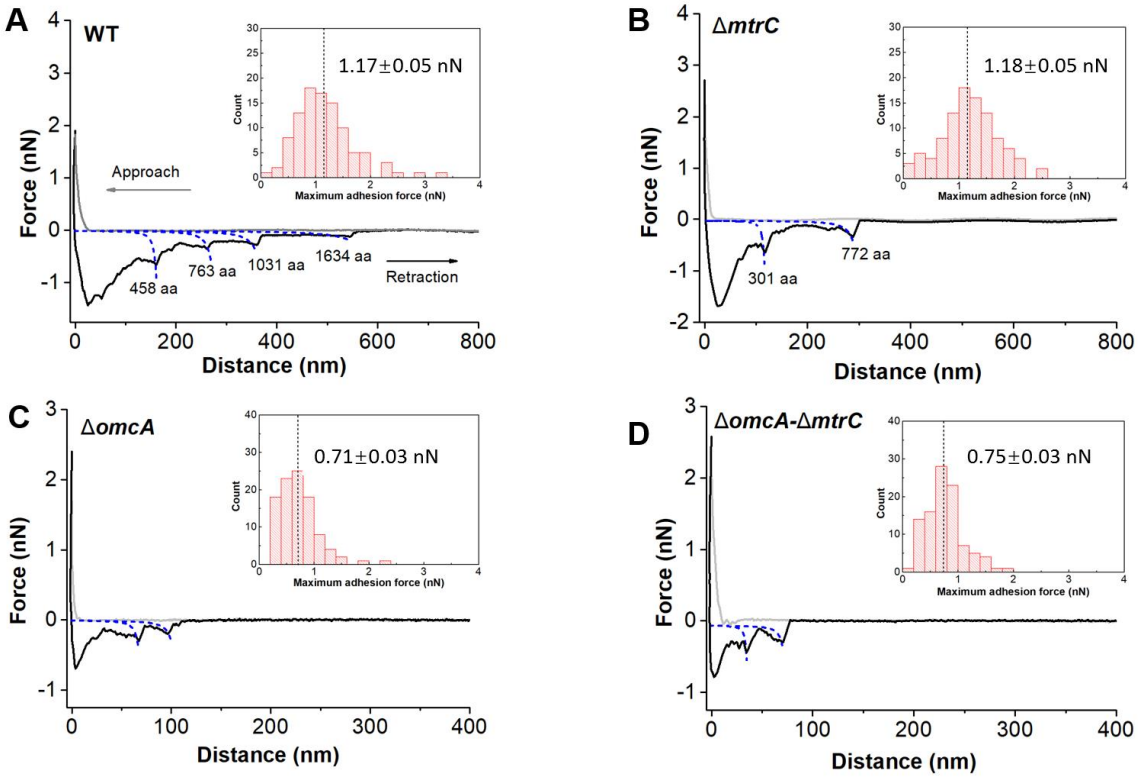

Fig. 8. Representative force-distance curves between WT (A), Δ*mtrC* (B), Δ*omcA* (C) and Δ*omcA*-Δ*mtrC* (D) and goethite under anaerobic conditions. Inset shows the adhesion force distribution of 100 measurements.

The sawtooth-like patterns in the retraction curves were analyzed to gain more definitive evidence for the role of OmcA and MtrC in the adhesion between *S. oneidensis* MR-1 and goethite. A single OmcA molecule composed of 748 amino acids corresponds to a contour

length of 299 nm, while a single MtrC molecule composed of 692 amino acids has a contour length of 277 nm (15). Based on the prediction of the worm-like chain (WLC) model, the rupture events for WT and Δ*mtrC* at about 291 nm (Fig. 8A) and 293 nm (Fig. 8B) are close to the contour length of OmcA, and 18 and 14% of the retraction curves (n=100) for WT and Δ*mtrC*, respectively, exhibit the sawtooth-shaped force signature of OmcA. On the other hand, the frequency of MtrC rupture events for WT and Δ*omcA* is only 9% and 3%, respectively. Therefore, these results indicate that OmcA is central in the short-term interaction between *S. oneidensis* MR-1 and goethite, and its involvement in these interactions enhances the attractive force by about 60% (Table S10). This stronger binding force can induce more attachment, which correlates with more WT and Δ*mtrC* cells attached on goethite in the initial attachment phase (Fig. 2).

DISCUSSION

Role of outer membrane *c*-Cyts in *S. oneidensis* Attachment to Goethite. Based on the QCM-D dissipation shift (Δ*D*) there appears to be three stages of attachment to the goethite surface for WT and mutants. All bacterial cells undergo a period of initial attachment, but this appears to be enhanced for WT and the mutant lacking MtrC, Δ*mtrC,* compared to the mutant lacking OmcA, Δ*omcA,* and lacking both OmcA and MtrC, Δ*omcA*-Δ*mtrC*. This result indicates that OmcA is important in the initial attachment phase. After this initial attachment, there appears to be a transition in the type and/or number of bacterial attachments, with all the strains except Δ*mtrC* showing a substantial increase in the amount of attached cells. This suggests that OmcA is somewhat less important than MtrC in the longer-term interactions of

337 the cells with the goethite surfaces. In the third and final attachment phase there appears to be
338 a relatively stable assemblage of cells attached to the goethite surface.

339 To further elucidate the relative importance of OmcA and MtrC in the initial and
340 subsequent stages of cell attachment, the viscoelastic properties of surface-associated cells
341 can be evaluated via the slope of ΔD-Δf plots (22, 25). A flat slope indicates a rigid mass
342 attachment (25). In the final attachment stage, WT displays overlapping and flat slopes at
343 overtones higher than 3 (Fig. S7). As the 3rd, 5th, 7th and 9th overtones correspond to ~144, 110,
344 94 and 83 nm sensing depths (25), the overlapping slopes suggest that WT forms a rigid
345 bacterial layer with a thickness of about 110 nm. Consistent with the higher elastic constant,
346 the slope of Δ*omcA* is flatter than that of Δ*mtrC,* which indicates higher rigidity of the
347 attached bacteria (Fig. S7). As such, while OmcA is important in the initial stages of
348 attachment, MtrC may be effective in developing longer-term stable bonds with goethite,
349 which increase the rigidity of the attached bacteria and reduce the energy dissipation (ΔD).
350

351 **OmcA Promotes Rapid and Strong Bacterial Adhesion to Goethite.** Previous AFM
352 studies demonstrate that purified OmcA and MtrC form strong bonds with iron (hydr)oxide,
353 but that the binding strength of OmcA with iron (hydr)oxides is about twice that for MtrC (15,
354 17). Studies using single whole cells also reveal an absence of MtrC unfolding trajectory
355 during *Shewanella*-goethite interaction (33). Using multiple whole cells, the study here shows
356 that during the initial attachment phase, the mutant lacking MtrC, Δ*mtrC*, and thus possessing
357 OmcA, experiences considerable bacterial attachment and high cell densities at the goethite
358 surface, comparable to WT (Fig. 1 and 2). At the beginning of the second attachment stage

however, all the bacterial strains except Δ*mtrC* show a substantial increase in bacterial attachment, suggesting that while OmcA is important for initial attachment, it is somewhat less important for driving subsequent longer-term attachment (Fig. 2). During the initial attachment phase Δ*mtrC* also experiences the largest adhesion force between the bacteria and goethite surfaces, again comparable to WT (Fig. 8). The ATR-FTIR and 2D COS analysis suggest that P-moieties $\upsilon_s(PO_2^-)$ are primarily involved in the initial attachment of both WT and Δ*mtrC* (Fig. S5 and 6). Taken together these results indicate that the binding strength of OmcA is greater than MtrC during the initial attachment phase, which leads to a rapid and strong attachment of *S. oneidensis* MR-1 to the goethite surface, with MtrC contributing less to this short-term interaction. It should be noted that the AFM adhesion force measured in this study is slightly higher than that between single MR-1 cells and goethite (0.75 nN) (33). The difference may be ascribed to the binding of multiple cells with goethite surface.

MtrC Promotes Longer-Term Bacterial Adhesion to Goethite via Microbial P-moieties. Following the initial attachment phase, at the beginning of the second attachment phase, this study shows that all the bacterial strains except the mutant lacking MtrC, Δ*mtrC*, show a substantial increase in bacterial attachment (Fig. 2). Furthermore, the presence of MtrC is shown to enhance the contact area between *S. oneidensis* MR-1 and goethite, where a higher contact area results in higher elastic and damping effects during the cell-mineral interaction (Table 1). The differential effects of OmcA and MtrC may be associated with their different orientations on cell surfaces. OmcA and MtrC contain similar structure and heme arrangements, which can bind to iron oxides through their solvent-exposed hemes (4, 12). As

one of the solvent-exposed termini in MtrC was associated with periplasmic MtrA through transmembrane porin MtrB, MtrC was uniformly anchored and extended from the outer membrane surface (34-36). Meanwhile, the proper localization of OmcA on cell surface is assisted by MtrC without which OmcA attached to outer membrane merely via the N-terminal lipoprotein modification (37, 38). Therefore, OmcA on Δ*mtrC* may move via lateral diffusion and stabilize at *Shewanella*-goethite interface. The immunolocalization assay also demonstrates that lacking MtrC causes a significant reduction in the coverage of *c*-Cyts on cell surface (Fig. 5). It suggested that MtrC not only directly binds with goethite, but also influences the interaction between OmcA and goethite.

The ATR-FTIR and 2D COS analysis suggest that the mutant lacking OmcA, Δ*omcA*, and thus possessing MtrC, interacts with the goethite surface via P-moieties υ(P-OFe), forming inner-sphere monodentate Fe-phosphate/phosphonate surface complexes (Fig. 7). As such, it appears that after the initial attachment stage, MtrC promotes the attachment of *S. oneidensis* MR-1 to goethite, via the formation of Fe-phosphate/phosphonate surface complexes. It should be noted that while P-moieties υ(P-OFe) are involved to some extent in the initial binding of both WT and the mutant lacking OmcA, Δ*omcA*, and thus possessing MtrC, these do not provide the strongest adhesion during this first attachment step (Fig. 8C).

Overall based on *in situ* ATR-FTIR 2D-CoS analysis, the attachment process for both WT and mutants during the initial ($\upsilon_s(PO_2^-)$) and subsequent (υ(P-OFe)) attachment phases is initiated by phosphate-bearing groups at the bacterial cell surface. The affinity of bacterial P-moieties for iron (hydr)oxides are recognised for *S. putrefaciens*, *Pseudomonas aeruginosa* and *Bacillus subtilis* (28, 32). Interestingly, recent work characterizes the surface reaction

between *Shewanella* and iron (hydr)oxide under aerobic conditions (27, 32) and AFM analyses in particular demonstrate that the affinity between *Shewanella* and iron (hydr)oxides is significantly reduced under aerobic compared to anaerobic conditions (11, 33, 39). A possible explanation for the reduced affinity between the bacteria and mineral surface under aerobic conditions, might lie in the fact that the attachment process of WT under aerobic conditions is similar to those of Δ*mtrC* and Δ*omcA*-Δ*mtrC* under the anaerobic conditions of this study, in which phosphate groups react with goethite to play a central role in bacterial adhesion (27). Previous studies demonstrated that when *Shewanella* cells are exposed to oxygen, *c*-Cyts become embedded in the outer cell membrane (33, 40), such that their role in promoting initial attachment and longer-term binding via the phosphate groups is significantly reduced. Overall it appears that different binding affinities and interfacial reactions between bacteria and goethite under aerobic and anaerobic conditions might be mainly attributed to the specific roles of outer membrane *c*-Cyts.

Environmental Significance. Microbial dissimilatory iron reduction (DIR) is a fundamentally important process in subsurface soils and sediments, where it mediates the biogeochemical cycling of iron and carbon, but also impacts the reactivity and cycling of other essential bioelements and contaminants, through control of subsurface redox conditions (4). OmcA and MtrC are the terminal reductases on *Shewanella* cell surfaces that transfer electrons directly to solid minerals, which in turn drives DIR (1). Although the amount of OmcA and MtrC at the cell surface and their molecular structures are largely comparable, previous studies have shown that MtrC rather than OmcA plays a more central role in DIR (8,

20, 21). This study investigates the role of *c*-Cyts in whole cell interactions with the ubiquitous iron (hydr)oxide goethite. The results show that OmcA contributes to the initial attachment via strong binding force and MtrC enhances the contact area between bacteria and the goethite surface. As the high contact area associates with effective extracellular electron transfer (41-43), this study sheds new light on the indispensable function of MtrC in DIR. Overall this study shows that, besides transferring electrons, *c*-Cyts enhance the attachment of *Shewanella* cells onto iron (hydr)oxides via two different strategies, specific to either OmcA in the initial attachment stage and MtrC in the subsequent attachment stage. This outer membrane c-type cytochrome promoted rapid attachment and colonization of bacteria on iron (hydr)oxide minerals confers these strains a survival advantage in subsurface soils and sediments.

CONCLUSION

The outer membrane *c*-type cytochromes OmcA and MtrC are key terminal reductases for *Shewanella* cells to mediate extracellular electron transfer. Although previous studies on purified *c*-Cyts have revealed their similar structural properties, little is known about their roles in *Shewanella*-mineral interaction at the whole-cell level. This study demonstrates that OmcA and MtrC play distinct roles in *S. oneidensis* MR-1 attachment to goethite. OmcA contributes to 60% higher attractive force between bacterial cells and the goethite surface and induces a rapid short-term attachment. Meanwhile, MtrC enhances the contact area of bacterial cells with goethite by more than twofold and promotes the interfacial reaction and inner-sphere coordination between bacterial phosphate groups and the mineral surface. The

increased contact area offered by MtrC may explain its central role in extracellular electron transfer.

MATERIAL AND METHODS

Bacteria and Cultivation Media. Wild-type *S. oneidensis* MR-1 (WT) and three mutant strains (Δ*omcA*, Δ*mtrC* and Δ*mtrC*-Δ*omcA*) are described in previous studies (44). The phenotype and genotype of mutant strains were validated via PCR and immunolocalization (Fig. S8 and S9). The cells were pre-cultivated in Luria-Bertani (LB) medium under aerobic conditions at 30 °C. After overnight cultivation, the cells were washed three times and resuspended in 0.1 M NaCl solution to a concentration of 1×10^8 cells mL^{-1}.

Synthesis and Characterization of Goethite. Goethite was synthesized by following previously reported approaches (45, 46). Briefly, 0.15 M $Fe(NO_3)_3$ was added into 2.5 M KOH neutralizing solution. After aging for 24 h at 60 °C, the mineralogy and morphology of the synthetic goethite was verified by X-ray diffraction (XRD) and transmission electron microscopy (TEM) analysis (Fig. S10). The average size of the goethite particles is 195.8±42.9 nm.

QCM-D Analysis of Bacterial Attachment on Goethite. The adhesion process was examined by using a QCM-D system (Q-Sense, Sweden). To begin with, a thin layer of goethite was spin-coated on a gold-plated sensor. The attachment processes of WT and mutants on the bare gold sensor show no significant difference (Fig. S11). Then cell-free 0.1 M NaCl solution at pH 7.0 was injected for 4 h to establish a background signal. The bacterial solution (pH 7.0) was then introduced at a flow rate of 85 μL/min. Based on on-line pH measurement, the pH of bacterial suspension was kept constant at 7.0 by adding dilute HCl or

NaOH solution. The changes in oscillating frequency (Δf, Hz) and energy dissipation (ΔD) were recorded at 5 different overtones (n=3, 5, 7, 9 and 11). During the measurement, the bacterial suspension was purged with nitrogen gas to ensure anaerobic conditions. Due to the absence of electron donors, goethite was not reduced during bacterial attachment processes (Table S11). The cell viability was examined via Live/Dead BacLight bacterial viability kit L7012 (47). More than 98% of cells were alive after incubation in 0.1 M NaCl for 11 hours (Fig. S12). Bacteria adhered on the QCM-D sensor was stained with SYTO 9 and observed under a confocal laser scanning microscope (FV1000, Olympus, Japan). Five images for each strain were collected and the cell density was determined using IMARIS software (48).

Modeling of QCM data. A quantitative model of QCM-D response was applied to quantify the different interaction processes of *S. oneidensis* MR-1 with goethite at 10 h. The obtained Δf_n and ΔD_n were fitted to the model to obtain contact elasticity (κ_c), contact damping (ξ_c) and density of attached bacteria (N_p) (26). After bacteria attach on the QCM-D surface, the load impedance is changed by ΔZ_L^* and the complex frequency shift is given as $\Delta f^* = \Delta f + i\Delta\Gamma$. The frequency ($\Delta f_n$) and bandwidth shifts ($\Delta\Gamma_n$) at overtones n correspond to

$$\Delta f_n = -\frac{f_F}{\pi Z_q} Im(\Delta Z_L^*) \quad (1)$$

$$\Delta\Gamma_n = \frac{f_F n}{2}\Delta D_n = \frac{f_F}{\pi Z_q} Re(\Delta Z_L^*) \quad (2)$$

where f_F is the fundamental frequency which equals 5 MHz, ΔD_n is the dissipation shift at overtones n, Z_q is the acoustic impedance of an AT-cut quartz crystal (8.8×10^6 kg/(m^2·s)).

The proposed equivalent circuit considered that the total Δf_{total}^* is determined by the sum of the reciprocals of the contact region and oscillating particle loads (Fig. 4):

$$\Delta f_{total}{}^{*} = \left(\frac{1}{\Delta f_p^*} + \frac{1}{\Delta f_c^*}\right)^{-1} \quad (3)$$

where Δf_p^* and Δf_c^* are the frequency shifts for an oscillating particle and the contact region. Δf_p^* can be obtained as:

$$\Delta f_p^* = \Delta f_p + i\Delta\Gamma_p = \frac{N_p}{Z_q}\left[-\frac{8}{3}\pi R^3\left(\rho_p + \frac{\rho}{2}\right) {f_F}^2 n + i6\pi^{0.5} R^2 (\eta\rho)^{0.5} {f_F}^{1.5} n^{0.5}\right] \quad (4)$$

where ρ and η are the liquid density and viscosity (0.009 g/(cm·s)), R is the radius of bacteria (1 μm) and ρ_p is the bacterial density (1.348 g/cm^3) (26, 49).

The shift for contact region Δf_c^* is given as:

$$\Delta f_c^* = \Delta f_c + i\Delta\Gamma_c = N_p \frac{1}{1-\eta_r/\eta_t}\left[\frac{1}{2\pi^2 Z_q}\kappa_c n^{-1} + i\frac{f_F}{\pi Z_q}\xi_c n^0\right] \quad (5)$$

where η_t and η_r are the resistance coefficients for particle translation and rotation:

$$\eta_t = i\frac{4}{3}\pi R^3\left(\rho_p + \frac{\rho}{2}\right)\omega + 3\pi R^2\rho\delta\omega \quad (6)$$

$$\eta_r = i\frac{8}{15}\pi R^3\rho_p\omega + \frac{4}{3}\pi R^2\rho\delta\omega \quad (7)$$

ω is the angular oscillation frequency which equals to $2\pi n f_F$; δ is the penetration depth:

$$\delta = \left(\frac{\eta}{\pi\rho f_F}\right)^{0.5} n^{-0.5} \quad (8)$$

Nonlinear regression was performed to minimize the deviation (d) between experimental data (Δf_i^{exp} and $\Delta\Gamma_i^{exp}$) and predicated values:

$$d = \sqrt{\sum_i\left(\Delta f_i^{exp} - \Delta f_i^{model}\right)^2} + \sqrt{\sum_i\left(\Delta\Gamma_i^{exp} - \Delta\Gamma_i^{model}\right)^2} \quad (9)$$

Monte Carlo simulation was used to construct the 95% confidence intervals (50).

The radius of the contact region r_c can be derived from the fitted κ_c:

$$r_c = \left(\frac{3\kappa_c R^2}{4E_c}\right)^{1/3} \quad (10)$$

where E_c is the Young's modulus of the bacteria-substrate interface:

$$E_c = \left(\frac{1-v_p}{E_p} + \frac{1-v_s}{E_s}\right)^{-1} \quad (11)$$

and where v_p and E_p are the Poisson ratio and Young's modulus of *S. oneidensis* MR-1,

514 which are taken as 0.5 and 100 MPa, respectively (51). v_s and E_s for goethite equal 0.22
515 and 358 GPa, respectively (52).

516 **Immunolocalization of *c*-Cyts on cell surface.** The distribution of OmcA and MtrC
517 was revealed by immunolocalization assay. Affinity-purified antibodies toward the
518 hydrophilic and surface-exposed regions of MtrC and OmcA were prepared based on the
519 previous study (see supporting information for details) (44). *Shewanella* cells (4.8×10^7
520 cells/ml) were incubated with goethite (0.02 g/L) in 0.1 M NaCl solution anaerobically for 11
521 hours. The culture was then fixed in 4% paraformaldehyde for 15 min and washed with PBS
522 buffer. Goethite was dissolved by oxalic acid (15 g/L, pH=3.0) (53). After blocked in 1%
523 BSA solution, the samples were reacted with the primary antibody and secondary anti-rabbit
524 Alexa488 antibody sequentially. Cells were counterstained with
525 4′,6-diamidino-2-phenylindole (DAPI) and observed using structured illumination
526 microscopy (SIM, NIKON). Mander's overlap coefficient (MOC) was calculated to describe
527 the coverage of *c*-Cyts on cell surface in which higher MOC suggested higher coverage (54).
528 MOC was calculated as follows:

529 $$R = \frac{\sum_i S1_i \cdot S2_i}{\sqrt{\sum_i (S1_i)^2 \cdot \sum_i (S2_i)^2}} \quad (19)$$

530 where $S1_i$ represents signal intensity of the i^{th} pixel in the blue channel and $S2_i$ represents
531 signal intensity of the i^{th} pixel in the green channel.

532 **ATR-FTIR and 2D-CoS Analysis.** A Fourier transform infrared spectrometer (Bruker
533 IFS 66v/s) equipped with a liquid-nitrogen cooled detector was used for FTIR analysis. The
534 spectra were recorded over the range 400 to 4000 cm^{-1} with a resolution of 4 cm^{-1}. *In situ*

measurement of *S. oneidensis* MR-1 adhesion onto the goethite surface was conducted following previous studies (27, 32). Briefly, the goethite suspension was spread on the crystal surface of a ZnSe ATR flow cell. After drying for 12 h at 37 °C, a goethite film was formed on the ZnSe crystal. The cell-free 0.1 M NaCl solution was then injected into the flow cell to obtain a background spectrum. After 2 h, the bacterial suspension was pumped into the flow cell by a peristaltic pump at 1 mL/min. During the measurement, the bacterial suspension was purged with nitrogen gas to ensure anaerobic conditions and the pH was kept constant at 7.0 by adding a small amount of dilute HCl or NaOH. Spectra were recorded for 16 h until no further changes were observed. The ATR-FTIR spectra of the bacteria-goethite samples were obtained by subtracting the background spectrum.

The 2D correlation analysis of attached bacteria was performed by using 2D-Shige (Shigeaki Morita, Japan) (27, 55, 56). In this analysis, contact time was used as the external perturbation for the interaction of OMCs with goethite. The calculations were carried out by using Origin 8.5. An analytical spectrum $U(v, t)$ is considered to illustrate how the technique works. The variable v is the index variable for the FTIR spectra caused by the perturbation variable t. A discrete set of dynamic spectra measured at m equally spaced points in time t between T_{min} and T_{max} can be expressed by the following equation:

$$U_j(v) = y(v, t_j), j = 1, 2, \ldots, m \quad (12)$$

A set of dynamic spectra can be represented as follows:

$$\tilde{\mathrm{U}}(v, t) = U(v, t_j) - \bar{\mathrm{U}}(v) \quad (13)$$

where $\bar{\mathrm{U}}(v)$ represents the reference spectrum, which is the average spectrum and can be calculated as follows:

$$\bar{U}(v) = \frac{1}{m}\sum_{j=1}^{m} U(v, t_j) \tag{14}$$

The synchronous correlation intensity can be directly gained by the following equation:

$$\Phi(v_1, v_2) = \frac{1}{m-1}\sum_{j=1}^{m} \tilde{U}_j(v_1)\tilde{U}_j(v_2) \tag{15}$$

The asynchronous correlation intensity can be obtained as follows:

$$\Psi(v_1, v_2) = \frac{1}{m-1}\sum_{j=1}^{m} \tilde{U}_j(v_1)\sum_{k=1}^{m} M_{jk}\,\tilde{U}_j(v_2) \tag{16}$$

The term M_{jk} corresponds to the j^{th} column and the k^{th} raw element of the discrete Hibert-Noda transformation matrix, which can be calculated as follows:

$$M_{jk} = \begin{cases} 0 & if\ j = k \\ \dfrac{1}{\pi(k-j)} & otherwise \end{cases} \tag{17}$$

The intensity of a synchronous correlation spectrum Φ (v_1, v_2) represents the simultaneous or coincidental changes of two separate spectral intensity variations measured at v_1 and v_2 during the interval between T_{min} and T_{max} of the externally defined variable *t*. The intensity of an asynchronous spectrum ψ (v_1, v_2) represents sequential or successive, but not coincidental, changes of spectral intensities measured separately at v_1 and v_2. The rank order of intensity change between two bands at v_1 and v_2 can be obtained from the signs of the synchronous correlation peak Φ (v_1, v_2) and asynchronous correlation peak ψ (v_1, v_2) based on previously established principles (56-58). Basically, the sign of the synchronous correlation peak Φ (ν1, ν2) is positive when the spectral intensities of band ν1 and band ν2 are either increasing or decreasing together during the observation period (t), otherwise, the sign is negative. For the asynchronous correlation peak Ψ (ν1, ν2), the sign is positive when the

change in the intensity of band ν1 occurs prior to that of band ν2, otherwise, the sign is negative. When Φ (ν1, ν2) and Ψ (ν1, ν2) having the same signs, the intensity change of band ν1 occurs predominantly before that of band ν2; when they having the opposite signs, the change order is reverse. The changes of band ν1 and band ν2 occur simultaneously when Ψ (ν1, ν2) equals to zero (56-58).

As the changes in spectral intensity represent the interaction of the corresponding IR bands and outer membrane *c*-Cyts functional groups, the order in which the spectral intensity changes reflects the sequence in which the IR bands and the corresponding outer membrane *c*-Cyts functional groups interact with the goethite surface. In this way the results obtained from the 2D-CoS can reflect the order in which the different outer membrane *c*-Cyts functional groups interact and bind with goethite.

AFM analysis of adhesion force. Prior to adhesion of bacteria on the AFM cantilever, 6.1 μm-radius silica beads (Bangs Laboratories) were rinsed with deionized water and dried on a glass slide. The beads were mounted onto a triangular tipless AFM cantilever (Bruker) coated with UV curable glue (Adhesive 63, Norland Products) (59). After 30-min UV exposure, the colloidal probe was washed with ethanol and deionized water. The rinsed probe was immersed into 0.01% poly-L-lysine (Sigma) solution for 1 min to yield a positively charged surface. Then the cantilever was dipped into the bacterial suspension (1×10^{10} cell/mL) for 1 min to immobilize bacteria on the silica beads. The goethite substratum was prepared as previously described (60). Briefly, 0.4 mL of goethite suspension (1 g/L) was pipette onto a glass slide and then dried at 120 °C. After rinsing in deionized water, the goethite-coated slide was sterilized by autoclaving. The force measurement was conducted using a MultiMode 8

AFM system with a NanoScope V controller (Bruker). The mechanical data were obtained in the contact mode in N_2-purged 0.1 M NaCl solution at a scan rate of 1 Hz. The ramp size was 1 μm and the trigger threshold was 2 nN. A contact time of 10 s was used. The worm-like chain (WLC) model was used to estimate the retraction curve for bacterial surface biopolymers. The theoretical force-extension $F(D)$ relationship is given as:

$$F(D) = \left(\frac{k_B T}{p}\right) \cdot [0.25(1 - \frac{D}{L})^{-2} + \frac{D}{L} - 0.25] \quad (18)$$

where D is the extension, k_B is the Boltzmann contant (1.38×10^{-23} J/K), T is the temperature (in K), p is the persistence length and L is the biopolymer's contour length (61).

Statistics. All attachment experiments were performed in triplicate. Statistical analysis was performed via the student's *t*-test. A *P* value higher than 0.05 indicates no significant difference within the 95% confidence interval.

ACKNOWLEDGMENTS

This work was supported by the National Natural Science Foundation of China (41807024), National Basic Research Program of China (2016YFD0800206), Fundamental Research Funds for the Central Universities (Program No. 52902-0900201674) and Royal Society Newton Advance Fellowship (NAF/R1/191017).

RESEARCH DATA

Research data associated with this article can be access at http://dx.doi.org/10.17632/6d3kx7m6ms.1

The authors declare no competing financial interest.

REFERENCES

1. Lovley DR. 1991. Dissimilatory Fe (III) and Mn (IV) reduction. Microbiol Mol Biol Rev 55:259-287.
2. Schwertmann U. 1993. Relations between iron oxides, soil color, and soil formation. Soil color:51-69.
3. Ponnamperuma FN. 1972. The chemistry of submerged soils, p 29-96, Advances in agronomy, vol 24. Elsevier.
4. Shi L, Dong H, Reguera G, Beyenal H, Lu A, Liu J, Yu HQ, Fredrickson JK. 2016. Extracellular electron transfer mechanisms between microorganisms and minerals. Nat Rev Microbiol 14:651-662.
5. Fredrickson JK, Romine MF, Beliaev AS, Auchtung JM, Driscoll ME, Gardner TS, Nealson KH, Osterman AL, Pinchuk G, Reed JL, Rodionov DA, Rodrigues JL, Saffarini DA, Serres MH, Spormann AM, Zhulin IB, Tiedje JM. 2008. Towards environmental systems biology of *Shewanella*. Nat Rev Microbiol 6:592-603.
6. Shi L, Rosso KM, Clarke TA, Richardson DJ, Zachara JM, Fredrickson JK. 2012. Molecular Underpinnings of Fe(III) Oxide Reduction by *Shewanella Oneidensis* MR-1. Front Microbiol 3:50.
7. Mitchell AC, Peterson L, Reardon CL, Reed SB, Culley DE, Romine MR, Geesey GG. 2012. Role of outer membrane *c*-type cytochromes MtrC and OmcA in *Shewanella oneidensis* MR-1 cell production, accumulation, and detachment during respiration on hematite. Geobiology 10:355-370.
8. Bretschger O, Obraztsova A, Sturm CA, Chang IS, Gorby YA, Reed SB, Culley DE, Reardon CL, Barua S, Romine MF, Zhou J, Beliaev AS, Bouhenni R, Saffarini D, Mansfeld F, Kim BH, Fredrickson JK, Nealson KH. 2007. Current production and metal oxide reduction by *Shewanella oneidensis* MR-1 wild type and mutants. Appl Environ Microbiol 73:7003-7012.
9. Ross DE, Brantley SL, Tien M. 2009. Kinetic characterization of OmcA and MtrC, terminal reductases involved in respiratory electron transfer for dissimilatory iron reduction in *Shewanella oneidensis* MR-1. Appl Environ Microbiol 75:5218-5226.
10. Borloo J, Vergauwen B, De Smet L, Brige A, Motte B, Devreese B, Van Beeumen J. 2007. A kinetic approach to the dependence of dissimilatory metal reduction by *Shewanella oneidensis* MR-1 on the outer membrane cytochromes *c* OmcA and OmcB. FEBS J 274:3728-3738.
11. Lower BH, Yongsunthon R, Shi L, Wildling L, Gruber HJ, Wigginton NS, Reardon CL, Pinchuk GE, Droubay TC, Boily JF, Lower SK. 2009. Antibody recognition force microscopy shows that outer membrane cytochromes OmcA and MtrC are expressed on the exterior surface of *Shewanella oneidensis* MR-1. Appl Environ Microbiol 75:2931-2935.
12. Shi L, Richardson DJ, Wang Z, Kerisit SN, Rosso KM, Zachara JM, Fredrickson JK. 2009. The roles of outer membrane cytochromes of *Shewanella* and *Geobacter* in extracellular electron transfer. Environ Microbiol Rep 1:220-227.
13. Lower BH, Lins RD, Oestreicher Z, Straatsma TP, Hochella MF, Shi LA, Lower SK. 2008. In vitro evolution of a peptide with a hematite binding motif that may constitute a natural

metal-oxide binding archetype. Environ Sci Technol 42:3821-3827.
14. Edwards MJ, Baiden NA, Johs A, Tomanicek SJ, Liang L, Shi L, Fredrickson JK, Zachara JM, Gates AJ, Butt JN, Richardson DJ, Clarke TA. 2014. The X-ray crystal structure of *Shewanella oneidensis* OmcA reveals new insight at the microbe-mineral interface. FEBS Lett 588:1886-1890.
15. Lower BH, Shi L, Yongsunthon R, Droubay TC, McCready DE, Lower SK. 2007. Specific bonds between an iron oxide surface and outer membrane cytochromes MtrC and OmcA from *Shewanella oneidensis* MR-1. J Bacteriol 189:4944-4952.
16. Sheng A, Liu F, Shi L, Liu J. 2016. Aggregation Kinetics of Hematite Particles in the Presence of Outer Membrane Cytochrome OmcA of *Shewanella oneidenesis* MR-1. Environ Sci Technol 50:11016-11024.
17. Xiong Y, Shi L, Chen B, Mayer MU, Lower BH, Londer Y, Bose S, Hochella MF, Fredrickson JK, Squier TC. 2006. High-affinity binding and direct electron transfer to solid metals by the *Shewanella oneidensis* MR-1 outer membrane *c*-type cytochrome OmcA. J Am Chem Soc 128:13978-13979.
18. Liu J, Pearce CI, Shi L, Wang Z, Shi Z, Arenholz E, Rosso KM. 2016. Particle size effect and the mechanism of hematite reduction by the outer membrane cytochrome OmcA of *Shewanella oneidensis* MR-1. Geochimica et Cosmochimica Acta 193:160-175.
19. Ross DE, Brantley SL, Tien M. 2009. Kinetic Characterization of OmcA and MtrC, Terminal Reductases Involved in Respiratory Electron Transfer for Dissimilatory Iron Reduction in *Shewanella oneidensis* MR-1. Appl Environ Microbiol 75:5218-5226.
20. Myers JM, Myers CR. 2001. Role for outer membrane cytochromes OmcA and OmcB of *Shewanella putrefaciens* MR-1 in reduction of manganese dioxide. Appl Environ Microbiol 67:260-269.
21. Coursolle D, Gralnick JA. 2010. Modularity of the Mtr respiratory pathway of *Shewanella oneidensis* strain MR-1. Mol Microbiol 77:995-1008.
22. Kao WL, Chang HY, Lin KY, Lee YW, Shyue JJ. 2018. Assessment of the Effects of Surface Potential on the Kinetics of HEK293T Cell Adhesion Behavior Using a Quartz Crystal Microbalance with Dissipation Monitoring. J Phys Chem C 122:694-704.
23. Sadman K, Wiener CG, Weiss RA, White CC, Shull KR, Vogt BD. 2018. Quantitative Rheometry of Thin Soft Materials Using the Quartz Crystal Microbalance with Dissipation. Anal Chem 90:4079-4088.
24. Kao WL, Chang HY, Lin KY, Lee YW, Shyue JJ. 2018. Assessment of the Effects of Surface Potential on the Kinetics of HEK293T Cell Adhesion Behavior Using a Quartz Crystal Microbalance with Dissipation Monitoring. Journal of Physical Chemistry C 122:694-704.
25. Kao WL, Chang HY, Lin KY, Lee YW, Shyue JJ. 2017. Effect of Surface Potential on the Adhesion Behavior of NIH3T3 Cells Revealed by Quartz Crystal Microbalance with Dissipation Monitoring (QCM-D). J Phys Chem C 121:533-541.
26. Tarnapolsky A, Freger V. 2018. Modeling QCM-D Response to Deposition and Attachment of Microparticles and Living Cells. Anal Chem 90:13960-13968.
27. Yan W, Wang H, Jing C. 2016. Adhesion of *Shewanella oneidensis* MR-1 to Goethite: A Two-Dimensional Correlation Spectroscopic Study. Environ Sci Technol 50:4343-4349.
28. Parikh SJ, Chorover J. 2006. ATR-FTIR spectroscopy reveals bond formation during bacterial adhesion to iron oxide. Langmuir 22:8492-8500.

29. Elzinga EJ, Huang JH, Chorover J, Kretzschmar R. 2012. ATR-FTIR Spectroscopy Study of the Influence of pH and Contact Time on the Adhesion of *Shewanella putrefaciens* Bacterial Cells to the Surface of Hematite. Environ Sci Technol 46:12848-55.
30. Omoike A, Chorover J, Kwon KD, Kubicki JD. 2004. Adhesion of Bacterial Exopolymers to α-FeOOH: Inner-Sphere Complexation of Phosphodiester Groups. Langmuir 20:11108-11114.
31. Jiang W, Saxena A, Song B, Ward BB, Beveridge TJ, Myneni SCB. 2004. Elucidation of functional groups on gram-positive and gram-negative bacterial surfaces using infrared spectroscopy. Langmuir 20:11433-11442.
32. Elzinga EJ, Huang JH, Chorover J, Kretzschmar R. 2012. ATR-FTIR spectroscopy study of the influence of pH and contact time on the adhesion of *Shewanella putrefaciens* bacterial cells to the surface of hematite. Environ Sci Technol 46:12848-12855.
33. Lower SK, Hochella MF, Beveridge TJ. 2001. Bacterial recognition of mineral surfaces: nanoscale interactions between *Shewanella* and α-FeOOH. Science 292:1360-1363.
34. Nakano CM, Byun HS, Ma H, Wei T, El-Naggar MY. 2015. A framework for stochastic simulations and visualization of biological electron-transfer dynamics. Comput Phys Commun 193:1-9.
35. Clarke TA, Edwards MJ, Gates AJ, Hall A, White GF, Bradley J, Reardon CL, Shi L, Beliaev AS, Marshall MJ, Wang Z, Watmough NJ, Fredrickson JK, Zachara JM, Butt JN, Richardson DJ. 2011. Structure of a bacterial cell surface decaheme electron conduit. Proc Natl Acad Sci USA 108:9384-9389.
36. Edwards MJ, White GF, Lockwood CW, Lawes MC, Martel A, Harris G, Scott DJ, Richardson DJ, Butt JN, Clarke TA. 2018. Structural modeling of an outer membrane electron conduit from a metal-reducing bacterium suggests electron transfer via periplasmic redox partners. J Biol Chem 293:8103-8112.
37. Paquete CM, Fonseca BM, Cruz DR, Pereira TM, Pacheco I, Soares CM, Louro RO. 2014. Exploring the molecular mechanisms of electron shuttling across the microbe/metal space. Front Microbiol 5:318.
38. Johs A, Shi L, Droubay T, Ankner JF, Liang L. 2010. Characterization of the decaheme *c*-type cytochrome OmcA in solution and on hematite surfaces by small angle x-ray scattering and neutron reflectometry. Biophys J 98:3035-3043.
39. Roberts JA, Fowle DA, Hughes BT, Kulczycki E. 2006. Attachment Behavior of *Shewanella putrefaciens* onto Magnetite under Aerobic and Anaerobic Conditions. Geomicrobiol J 23:631-640.
40. Sokolov I, Smith DS, Henderson GS, Gorby YA, Ferris FG. 2001. Cell surface electrochemical heterogeneity of the Fe(III)-reducing bacteria *Shewanella putrefaciens*. Environ Sci Technol 35:341-347.
41. Yan B, Wrenn BA, Basak S, Biswas P, Giammar DE. 2008. Microbial Reduction of Fe(III) in Hematite Nanoparticles by *Geobacter sulfurreducens*. Environ Sci Technol 42:6526-6531.
42. Bose S, Hochella MF, Gorby YA, Kennedy DW, McCready DE, Madden AS, Lower BH. 2009. Bioreduction of hematite nanoparticles by the dissimilatory iron reducing bacterium *Shewanella oneidensis* MR-1. Geochim Cosmochim Acta 73:962-976.
43. Roden EE, Zachara JM. 1996. Microbial Reduction of Crystalline Iron(III) Oxides: Influence of Oxide Surface Area and Potential for Cell Growth. Environ Sci

Technol 30:1618-1628.
44. Marshall MJ, Beliaev AS, Dohnalkova AC, Kennedy DW, Shi L, Wang Z, Boyanov MI, Lai B, Kemner KM, McLean JS, Reed SB, Culley DE, Bailey VL, Simonson CJ, Saffarini DA, Romine MF, Zachara JM, Fredrickson JK. 2006. *c*-Type Cytochrome-Dependent Formation of U(IV) Nanoparticles by *Shewanella oneidensis*. PLOS Biology 4:e268.
45. Atkinson R, Posner A, Quirk JP. 1967. Adsorption of potential-determining ions at the ferric oxide-aqueous electrolyte interface. J Phys Chem C 71:550-558.
46. Lin D, Cai P, Peacock CL, Wu Y, Gao C, Peng W, Huang Q, Liang W. 2018. Towards a better understanding of the aggregation mechanisms of iron (hydr) oxide nanoparticles interacting with extracellular polymeric substances: Role of pH and electrolyte solution. Sci Total Environ 645:372-379.
47. Wu Y, Mohanty A, Chia WS, Cao B. 2016. Influence of 3-Chloroaniline on the Biofilm Lifestyle of *Comamonas testosteroni* and Its Implications on Bioaugmentation. Appl Environ Microbiol 82:4401-4409.
48. Wu Y, Zaiden N, Liu X, Mukherjee M, Cao B. 2020. Responses of Exogenous Bacteria to Soluble Extracellular Polymeric Substances in Wastewater: A Mechanistic Study and Implications on Bioaugmentation. Environ Sci Technol 54:6919-6928.
49. Lewis K, Tzilivakis J, Green A, Warner D. 2013. Bio-pesticides database (BPDB). http://sitem.herts.ac.uk/aeru/ppdb/en/index.htm. Accessed July 26, 2019.
50. Lambert RJW, Mytilinaios I, Maitland L, Brown AM. 2012. Monte Carlo simulation of parameter confidence intervals for non-linear regression analysis of biological data using Microsoft Excel. Comput Meth Programs Biomed 107:155-163.
51. Tuson HH, Auer GK, Renner LD, Hasebe M, Tropini C, Salick M, Crone WC, Gopinathan A, Huang KC, Weibel DB. 2012. Measuring the stiffness of bacterial cells from growth rates in hydrogels of tunable elasticity. Mol Microbiol 84:874-891.
52. Chicot D, Mendoza J, Zaoui A, Louis G, Lepingle V, Roudet F, Lesage J. 2011. Mechanical properties of magnetite (Fe_3O_4), hematite (α-Fe_2O_3) and goethite (α-FeO·OH) by instrumented indentation and molecular dynamics analysis. Mater Chem Phys 129:862-870.
53. Reardon CL, Dohnalkova AC, Nachimuthu P, Kennedy DW, Saffarini DA, Arey BW, Shi L, Wang Z, Moore D, McLean JS, Moyles D, Marshall MJ, Zachara JM, Fredrickson JK, Beliaev AS. 2010. Role of outer-membrane cytochromes MtrC and OmcA in the biomineralization of ferrihydrite by *Shewanella oneidensis* MR-1. Geobiology 8:56-68.
54. Zinchuk V, Zinchuk O, Okada T. 2007. Quantitative colocalization analysis of multicolor confocal immunofluorescence microscopy images: pushing pixels to explore biological phenomena. Acta Histochem Cytochem 40:101-11.
55. Schmidt MP, Martínez CE. 2016. Kinetic and conformational insights of protein adsorption onto montmorillonite revealed using in situ ATR-FTIR/2D-COS. Langmuir 32:7719-7729.
56. Cai P, Lin D, Peacock CL, Peng W, Huang Q. 2018. EPS adsorption to goethite: Molecular level adsorption mechanisms using 2D correlation spectroscopy. Chem Geol 494:127-135.
57. Domínguez-Vidal A, Saenz-Navajas MP, Ayora-Cañada MJ, Lendl B. 2006. Detection of albumin unfolding preceding proteolysis using Fourier transform infrared spectroscopy

and chemometric data analysis. Anal Chem 78:3257-3264.
58. Jia Q, Wang N-N, Yu Z-W. 2009. An insight into sequential order in two-dimensional correlation spectroscopy. Appl Spectrosc 63:344-353.
59. Li X, Logan BE. 2004. Analysis of bacterial adhesion using a gradient force analysis method and colloid probe atomic force microscopy. Langmuir 20:8817-8822.
60. Huang Q, Wu H, Cai P, Fein JB, Chen W. 2015. Atomic force microscopy measurements of bacterial adhesion and biofilm formation onto clay-sized particles. Sci Rep 5:16857.
61. Janshoff A, Neitzert M, Oberdörfer Y, Fuchs H. 2000. Force spectroscopy of molecular systems-single molecule spectroscopy of polymers and biomolecules. Angew Chem Int Edit 39:3212-3237.

Figure legends

Fig. 1. The frequency (Δf) and dissipation (ΔD) shift for the attachment of WT (A), Δ*mtrC* (B), Δ*omcA* (C) and Δ*omcA*-Δ*mtrC* (D) on goethite-coated QCM-D sensors. I, II and III are different stages of bacterial attachment based on the changes of ΔD. f_n and D_n indicate the frequency and dissipation at 4 different overtones.

Fig. 2. WT (A, F), Δ*mtrC* (B, G), Δ*omcA* (C, H) and Δ*omcA*-Δ*mtrC* (D, I) after 2 and 4 hour attachment on goethite surfaces. The surface cell density is determined by statistical image analysis (E).

Fig. 3. Experimental and predicted Δf and $\Delta\Gamma$ as a function of the overtone number for WT (A, E), Δ*mtrC* (B, F), Δ*omcA* (C, G) and Δ*omcA*-Δ*mtrC* (D, H).

Fig. 4. The proposed equivalent circuits for the load impedance of the crystal associated with a single attached bacterial cell showing the overtone dependence of inertial, viscous, elastic and dissipative loads.

Fig. 5. Immunolocalization images of outer membrane *c*-Cyts OmcA and MtrC on cell surface of WT (A, C), Δ*mtrC* (C), Δ*omcA* (D) stained by DAPI (blue). Outer membrane *c*-Cyts OmcA and MtrC were specific labeled with antibodies against OmcA (A and C, green) or MtrC (B and D, green).

Fig. 6. Synchronous (A, C) and asynchronous (B, D) 2D correlation map of time-dependent ATR-FTIR spectra for the short-term (A, B) and long-term (C, D) attachment of Δ*mtrC* cells to goethite. The red and blue regions represent positive and negative correlation intensities.

Fig. 7. Synchronous (A, C) and asynchronous (B, D) 2D correlation map of time-dependent ATR-FTIR spectra for the short-term (A, B) and long-term (C, D) attachment of Δ*omcA* cells to goethite. The red and blue regions represent positive and negative correlation intensities.

Fig. 8. Representative force-distance curves between WT (A), Δ*mtrC* (B), Δ*omcA* (C) and Δ*omcA*-Δ*mtrC* (D) and goethite under anaerobic conditions. Inset shows the adhesion force distribution of 100 measurements.

836 Table 1. Fitted parameters for *Shewanella* attachment on goethite

Strain	κ_c (N m^{-1})	ξ_c (10^{-8} Pa m s)	N_p (10^5 cm^{-2}) [a]	r_c (nm) [b]	d
WT	41.13 (41.11-41.15) [c]	506.15 (481.39-539.51)	1.20 (1.19-1.22)	536.37 (536.27-536.45)	92.66
Δ*mtrC*	11.76 (11.75-11.78)	150.96 (145.67-155.58)	1.99 (1.95-2.04)	353.39 (353.22-353.55)	266.15
Δ*omcA*	27.67 (27.65-27.69)	336.42 (322.95-351.24)	1.21 (1.19-1.22)	469.99 (469.87-470.09)	112.79
Δ*omcA*-Δ*mtrC*	7.40 (7.39-7.42)	101.17 (96.89-103.88)	1.68 (1.64-1.73)	302.79 (302.63-303.01)	178.39

837 [a] N_p: Density of attached cells

838 [b] r_c: Radius of contact region for single attached cells

839 [c] 95% confidence region of parameters is presented in brackets.